Available online at www.sciencedirect.com
ScienceDirect
Solid State Communications 139 (2006) 605–616
solid state communications
www.elsevier.com/locate/ssc

Dynamics of rotating suspensions

W.R. Matson[a], B.J. Ackerson[a], P. Tong[b,*]

[a] Department of Physics, Oklahoma State University, Stillwater, OK 74078, United States
[b] Department of Physics, Hong Kong University of Science and Technology, Clear Water Bay, Kowloon, Hong Kong

Received 1 April 2006; accepted 11 April 2006 by P. Sheng
Available online 19 June 2006

Abstract

A suspension of non-Brownian settling particles in a completely filled horizontal rotating cylinder demonstrates a rich array of concentration and velocity patterns. Individual flow states, or phases, are studied using both side and cross-sectional imaging to examine the detailed flow structures. The overall steady state phase diagram of the system is mapped out as a function of the rotation rate and solvent viscosity. Theoretical attempts are made to understand the dynamics of the stable band phase in the rotating suspension.

PACS: 45.70.Qj; 05.65.+b; 83.10.Pp; 83.80.Hj

Keywords: A. Rotating suspensions; D. Pattern formation; D. Suspension dynamics; E. Video imaging

1. Introduction

Monodispersed colloidal suspensions are widely used as model systems to study the static and dynamic properties of soft matter [1]. The colloidal system consists of small uniform solid spheres suspended in a simple solvent. These small particles undergo vigorous Brownian motion in the solution and their spatial structure is determined primarily by the effective interaction potential $U(r)$ between the particles. This effective interaction potential takes all the solvent effects into account and thus the solvent does not appear explicitly in the description of the static properties of the suspension at thermal equilibrium. There is a variety of colloidal suspensions, whose interaction potential $U(r)$ varies from simple hard-sphere-like interaction and screened Coulomb repulsion to various short- or long-range attractions [2]. The exact form of $U(r)$ can be varied by changing the colloidal surface chemistry or the nature of the solvent. In the experiment, one obtains information about $U(r)$ by measuring either the particle pair correlation function $g(r)$, using optical and confocal microscopy, or the static structure factor $S(q)$ using the scattering techniques [2,3]. The variety of the interaction potentials leads to many interesting self-assembly structures, which have been studied intensively in recent years [4,5]. It also offers unique opportunities for the study of the phase behavior, from gas and liquid to crystal and various metastable and non-equilibrium states, such as gels and glasses [6–12].

In addition to the equilibrium structures, colloidal suspensions are also ideal systems for the study of non-equilibrium dynamics. First, they are soft and can be easily deformed by a weak external field. A typical modulus for a colloidal system is k_BT/a^3, where k_BT is the thermal energy and a is the radius of the particle [13]. The value of k_BT/a^3 for a suspension with $a = 1$ μm is approximately 10^{11} times smaller than the modulus for atomic systems. Second, the colloidal suspensions are slow and can be easily driven away from equilibrium by a simple shear or gravitational field. A typical relaxation time for a colloidal suspension is the time $t_d = a^2/D_0$ for a particle to diffuse over its own radius. Here $D_0 = k_BT/(6\pi\eta a)$ is the Stokes–Einstein diffusion constant for a single particle in a solvent of viscosity η. This time should be compared to a characteristic time $t_e \simeq a/U$ associated with the flow U produced by an external driving force. For example, heavy particles settle under gravity with the Stokes velocity $U_0 = 2\Delta\rho g a^2/(9\eta)$, where $\Delta\rho$ is the density difference between the particle and solvent and g is the gravitational acceleration. The ratio of the two time scales is called the Peclet number $Pe = t_d/t_e = aU/D_0$,

* Corresponding author.
E-mail address: penger@ust.hk (P. Tong).

0038-1098/$ - see front matter © 2006 Elsevier Ltd. All rights reserved.
doi:10.1016/j.ssc.2006.04.041

which determines when the suspension is driven out of equilibrium.

When $Pe < 1$, the system relaxes back to its equilibrium state faster than the time of changes imposed by the external driving force and thus the particle configurations remain the same as those at equilibrium, which are determined primarily by the thermodynamic interaction $U(r)$. When $Pe > 1$, the external force drives the system out of equilibrium and the particle configurations are coupled to the flow field. In this case, one has to consider the long-ranged hydrodynamic interactions mediated through the solvent, making the suspension dynamics an interesting and challenging problem in statistical physics and low-Reynolds-number hydrodynamics [2,14]. In addition to being soft and slow, which provides experimental convenience for control and manipulations, colloidal suspensions also offer an attraction of being visible under an optical microscope, allowing the use of various optical and video microscopy techniques for the measurement of the particle configurations and the (simultaneous) tracking of individual particle motions [15].

In this paper, we consider a non-equilibrium dynamic system, which consists of a settling suspension of uniform non-Brownian particles completely filling a horizontal rotating cylinder. The system is driven out of equilibrium by two external forces. First, because the particles chosen are relatively large ($a \simeq 100$ μm), they settle under gravity with a large settling velocity U_0. As a result, the Peclet number given by $Pe = aU_0/D_0$ is in the range between 6.5×10^8 and 1.2×10^{10}. This implies that the Brownian motion of the particles is negligible and the particle configurations are determined completely by the hydrodynamic interactions between the particles. Second, the entire system is under a uniform rotation, which provides an additional force to the particles. This force is proportional to the centripetal acceleration $\omega^2 r$ of the particles, where ω is the rotating rate of the cylinder and r is the radial position of the particles inside the cylinder.

Because of the imbalance between the solvent pressure gradient and the centrifugal force due to rotation, an individual (heavy) particle should not stay suspended in a rotating cylinder indefinitely. Roberts et al. [16] showed that a single particle inside a horizontal rotating cylinder will spiral outward continuously until it reaches the cell wall. The travelling time for the particle to reach the cell wall is given by

$$t_{\text{wall}} = \frac{g}{2U_0\omega^2} \ln\left(\frac{R^2 - x_0^2}{s^2}\right), \tag{1}$$

where R is the cylinder radius and s is the initial displacement from the spiral center x_0. The value of x_0 is obtained from the condition $x_0\omega = U_0$, under which the particle settling velocity U_0 is balanced by the upward rotation velocity $x_0\omega$. While the single-particle motion in a rotating cylinder is known with high precision, the collective behavior of the particles shows interesting but unexpected features. Recently, we carried out an experimental study of concentration and velocity patterns formed in a rotating suspension [17,18]. For our system with the solvent viscosity $\eta = 40$ centipoise (cP) and $\omega = 5.24$ 1/s, the

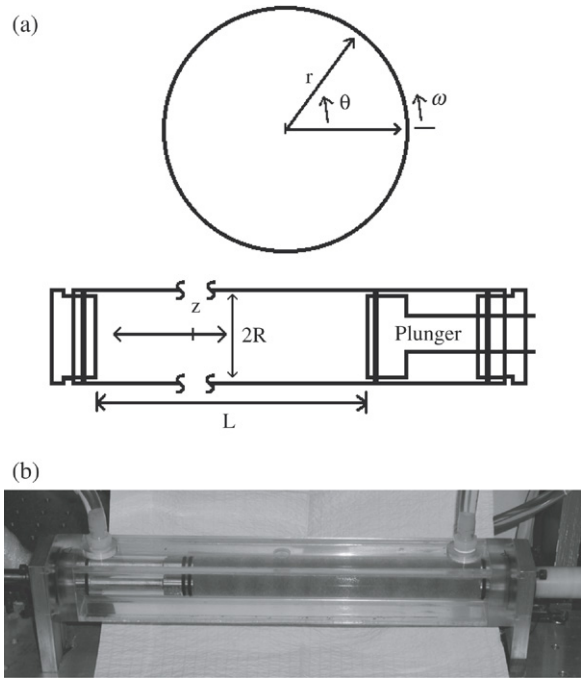

Fig. 1. (a) Construction of the rotating cylinder and the space coordinates used in the presentation of the measurements. (b) The actual experimental set-up.

travelling time t_{wall} is less than 10 min. Nevertheless, various concentration patterns were observed in the rotating suspension for several weeks without a noticeable change. The collective behavior of the particles was found to be qualitatively different from the single-particle dynamics.

In addition to its fundamental importance, the study of suspension dynamics is also related to a wide range of practical applications. Examples include the flow of mud, glass fibers in polymer solutions, sedimentation and transport of particles, as well as fluidization phenomena [19–21]. Understanding of the dynamics of rotating suspensions is required for computer modelling, process control, and various industrial applications of the rotating drum mixers, including the design of rotating reactors/mixers to minimize the sedimentation effect without using microgravity [16,22]. In the following, we first review the main experimental results obtained in the rotating suspension [17,18] and then present new dimensional analysis and theoretical calculation for the stable band phase found in the system.

2. Experiment

Fig. 1 shows the construction of the rotating cylinder and the actual experimental set-up. The rotating cylinder is made of a Plexiglas tube and is mounted horizontally on a thermally isolated aluminum stand. Details about the apparatus have been described elsewhere [18], and here we mention only some key points. The inner diameter of the tube is $2R = 1.91 \pm 0.04$ cm. Two Brass ends are milled to fit the tube and sealed with two o-rings. A sliding plunger is built similarly inside the tube, so that the length L of the tube to be filled in with a solution can be varied. Most measurements are carried out with a full tube length $L = 22.75 \pm 0.05$ cm. The cylinder rotates freely on ball

bearings inside a square cooling chamber, which has an inch of clearance around the cylinder. The temperature of the cooling chamber is maintained constant by circulating cold (hot) water from a temperature controlled bath/circulator. The temperature stability of the circulator is 0.05 °C, which provides fine control of the solvent viscosity. The cooling chamber is made of flat transparent Plexiglas plates to admit incident light and to observe the scattered light by the particles. The use of the flat window eliminates the optical distortions generated by the curvature of the cylinder sidewall and thus improves the quality of visualization of the concentration and velocity fields.

Fig. 1(a) also shows the space coordinates to be used below in the presentation of the measurements. The origin of the coordinate system is chosen to coincide with the center of the rotating cylinder. The r- and θ-axes are, respectively, the radial and azimuthal axes in the rotation plane and the z-axis is along the axis of symmetry (the rotation axis) of the cylinder. The cylinder is driven by a stepper motor. A thermally insulated coupler is used to prevent motor heat from entering the cylinder system. A micro-stepping drive controller regulates the motor position with a resolution of 2.5×10^4 steps/rotation. The controller is stimulated by a home-made indexer, which provides an accuracy of $2.5 \times 10^{-2} \pm 2.5 \times 10^{-5}$ s in the rotation period T. This fine control of the rotation period (or the rotation rate $\omega = 2\pi/T$) allows us to determine the boundary of each dynamic phase accurately.

The cylinder is filled completely with an aqueous solution of glycerin with a small amount of liquid detergent (0.25 vol.%) added to prevent particle aggregation. Two aqueous solutions of glycerin are used to cover a solution viscosity ranged from 8 to 100 cP. One aqueous solution has 60 wt.% mass concentration of glycerin and its viscosity varies from 8 to 22 cP when the temperature of the solution is changed from 30 °C to 5 °C. The other aqueous solution has 77 wt.% mass concentration of glycerin and its viscosity varies from 19 to 100 cP when the temperature of the solution is changed from 44 °C to 6 °C [23]. The particles used in the experiment are uniform glass spheres with an average density $\rho_p = 2.35$ g/cm^3. The particle radius is $a = 100$ μm and the size variation is less than 8%. The volume fraction of the particle suspension is fixed at $\phi = 0.023$. The density difference between the particle and the solvent is $\Delta\rho = \rho_p - \rho_s \simeq 1.19$ g/cm^3.

For solutions with viscosity ranged from 8 to 100 cP, the corresponding Stokes velocity U_0 varies from 3.25 to 0.26 mm/s. There are two length scales and two velocity scales in the problem, which give rise to four definitions of the Reynolds number. The Reynolds number based on the particle size and the settling velocity is given by $Re_1 = 2aU_0\rho_s/\eta$, which varies from 9.4×10^{-2} to 7.5×10^{-3} in the viscosity range mentioned above. The Reynolds number based on the particle size and wall speed, $Re_2 = 2aR\omega\rho_s/\eta$, ranges from 3 to 0.2 for a maximum rotation rate $\omega \simeq 4\pi$ (1/s). The Reynolds number based on the cylinder radius and wall speed, $Re_3 = R^2\omega\rho_s/\eta$, ranges from 1.7×10^2 to 13 for $\omega \simeq 4\pi$ (1/s). The Reynolds number based on the cylinder radius and the settling velocity is given by $Re_4 = RU_0\rho_s/\eta$, which varies from 2.9×10^{-2} to 4.5 in the viscosity range mentioned above.

In the experiment, we use a standard video imaging technique to record the motion and spatial distribution of the particles. A video charge-coupled-device (CCD) camera records particle images in different cross-sectional planes of the cylinder (r–θ plane) and in the vertical θ–z plane passing through the axis of rotation of the cylinder. To facilitate the imaging in the r–θ plane (end view), we construct a special short cell ($L = 2.25 \pm 0.03$ cm) with the same inner diameter but having a transparent end window for video imaging. A sheet of laser light of 1 mm in thickness is used to illuminate the r–θ plane of the cell. The whole cell is mounted on a translation stage, so that the flow visualization in the r–θ plane can be carried out at different locations along the z-axis. For the imaging of the long cylinder in the vertical θ–z plane (side view), back lit illumination is used. The particle trajectories are visible as streaks in superposed consecutive images. To vary the contrast of the particle images, we use both blue and translucent white glass spheres.

3. Experimental results

3.1. General phase behavior

The system exhibits a total of ten different steady states (or dynamic phases) and they are distinguished in the experiment by their unique flow patterns and particle distributions. At low rotation rates, the particles lie and slide on the bottom floor of the cylinder, forming a fluidized granular bed. At very high rotation rates, the centrifugal force becomes dominant and all the particles are spun onto the cylinder wall. Between the two extremes, we observed a series of interesting concentration and velocity patterns in the rotating suspension. Fig. 2 shows the "phase diagram" of the rotating suspension as a function of the rotation period $2\pi/\omega$ and solvent viscosity η. Here we briefly review each of the phases in order of their appearance with increasing ω. Detailed descriptions of the flow states can be found in Ref. [18]. Fig. 3 shows the side view of the particle distribution for different steady states. These images were taken using back lighting. Regions with higher particle population absorb and scatter more light and thus appear darker. Fig. 4 shows the cross-sectional view of particle trajectories for different steady states. For clarity, the contrast of the pictures is reversed with white streaks on a black background. The arrows indicate the direction of the local flow and the cylinder rotation.

Granular Bed (GB)

When ω is zero, the particles lie on the cylinder floor as a loosely packed granular bed. As the cylinder rotates, the bed is carried up along the rising wall. Under gravity the inner layer of particles in contact with the solvent slide downward, creating a circulation within the bed. A steady state is reached, which results in a fluidized granular flow similar in appearance to that observed for a viscous liquid in a partially filled rotating cylinder [24]. This gravity driven flow produces a counter rotation for the pure solvent in the central region of the cell. With larger ω, the top leading edge of the bed moves into the upper half of the cell and the particles are injected into and become suspended in the pure solvent region.

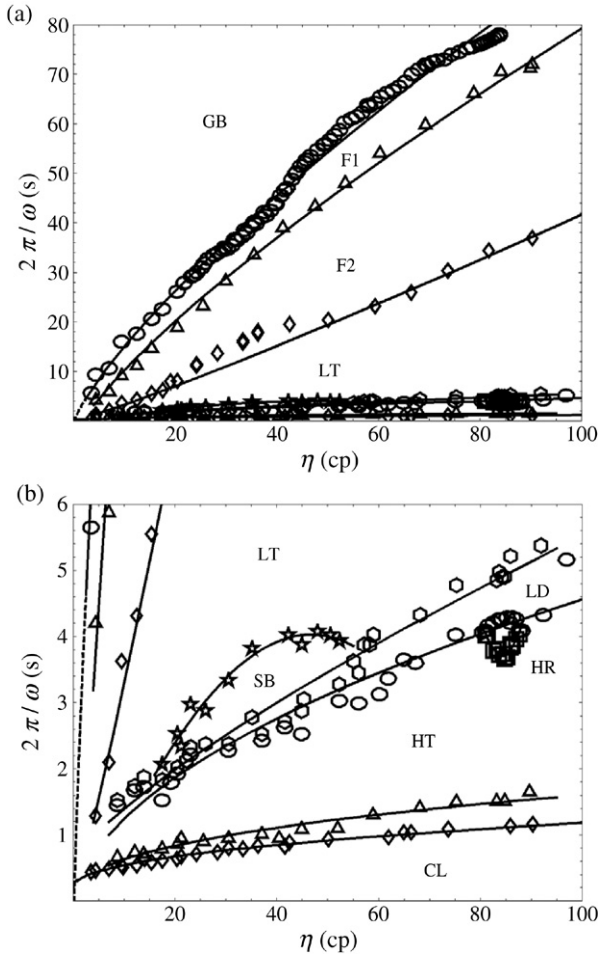

Fig. 2. (a) Overall phase diagram as a function of the rotation period $2\pi/\omega$ and solvent viscosity η. (b) An enlarged part of the phase diagram for high-rotation-rate states. The symbols are experimentally determined data points and the solid lines are spline-fitted smooth curves for the phase boundaries. The dashed lines are the extrapolated curves from the fit. GB: Granular Bed, F1: Fingering flow I, F2: Fingering flow II, LT: Low-rotation-rate Transition, SB: Stable Bands, LD: Local-structure Drop-off, HR: Homogeneous Region, HT: High-rotation-rate Transition, DB: Discontinuous Banding, and CL: Centrifugal Limit.

Fingering Flow I (F1)

Particles in the F1 phase behave differently from those in the GB phase on a microscopic level. In the GB phase, particles are mostly contained in the granular bed region. Those particles travelling near the upper part of the bed move downward together with the bed with the same velocity and they join the bed downstream in a relatively short period of time. In the F1 phase, however, particles leave the top, or leading edge of the bed, as a two-dimensional sheet. This is an unstable situation leading to a Rayleigh–Taylor-like instability. Particles clump together into lines or fingers. Initially, two or three particles line up loosely in the flow and then grow into chain-like structures of several millimeters in length and a few particle diameters in width. We call this "finger formation" and hence the resulting flow is named as "Fingering flow". As ω increases, the fingers grow both in number and size, and so does their settling velocity relative to the rotating background. The fingers distribute themselves along the z-axis uniformly. When a finger

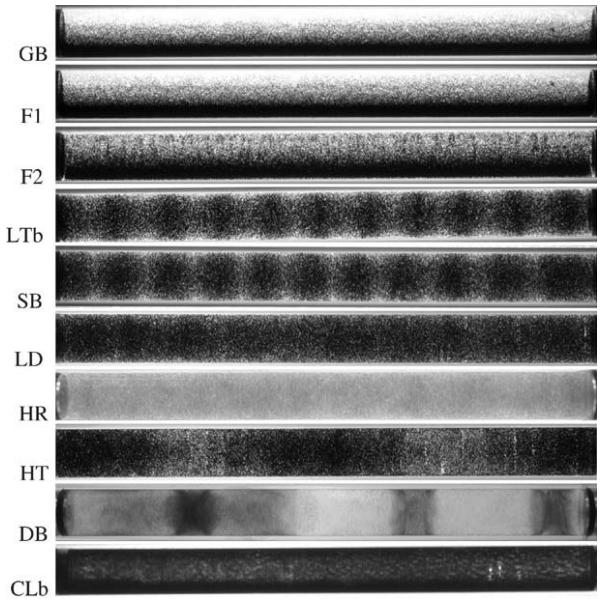

Fig. 3. Side view of the particle distribution in the long rotating cylinder. Darker regions have more particles. GB: Granular Bed, F1: Fingering flow I, F2: Fingering flow II, LTb: Low-rotation-rate Transition without a granular bed, SB: Stable Bands, LD: Local-structure Drop-off, HR: Homogeneous Region, HT: High-rotation-rate Transition, DB: Discontinuous Banding, and CLb: Centrifugal Limit with all particles on the cylinder wall.

falls, it follows the granular bed, keeping its radial position r nearly constant until it reaches the base of the bed.

Fingering Flow II (F2)

As mentioned above, the fingers become larger with increasing ω and thus produce larger disturbances to the flow field in the closed cylinder. The fingers in the F2 phase are large enough and become visible in the side view image shown in Fig. 3(F2). The thin vertical dark strands on the upper half of the tube are the growing fingers, which are distributed rather uniformly along the z-axis. These thin dark strands are invisible in Fig. 3(F1). Closer examination of the finger detachment near the top leading edge of the granular bed reveals that the fingers in the F1 phase detach from the rising wall at fixed locations of approximately equal distance along the cylinder when viewed from the side. In going from the F1 to F2 phases, we find that the detaching position of the settling fingers begins to drift over a small horizontal distance. As a result, the falling fingers when viewed at a fixed downstream location appear to have a zigzag-like trajectory as a function of time. Careful particle tracking reveals that the fingering flow is essentially two-dimensional independent of z in both the F1 and F2 phases.

Low-rotation-rate Transition (LT)

The onset of the Low-rotation-rate Transition is marked by the development of an axial component (v_z) of the finger velocity. The motion of the fingers becomes three-dimensional when the fingers start to fall toward the center of rotation at larger rotation rate. Further increasing ω results in the fingers falling next to the downward moving cylinder wall. Once this occurs, the granular bed is quickly dissolved and all the

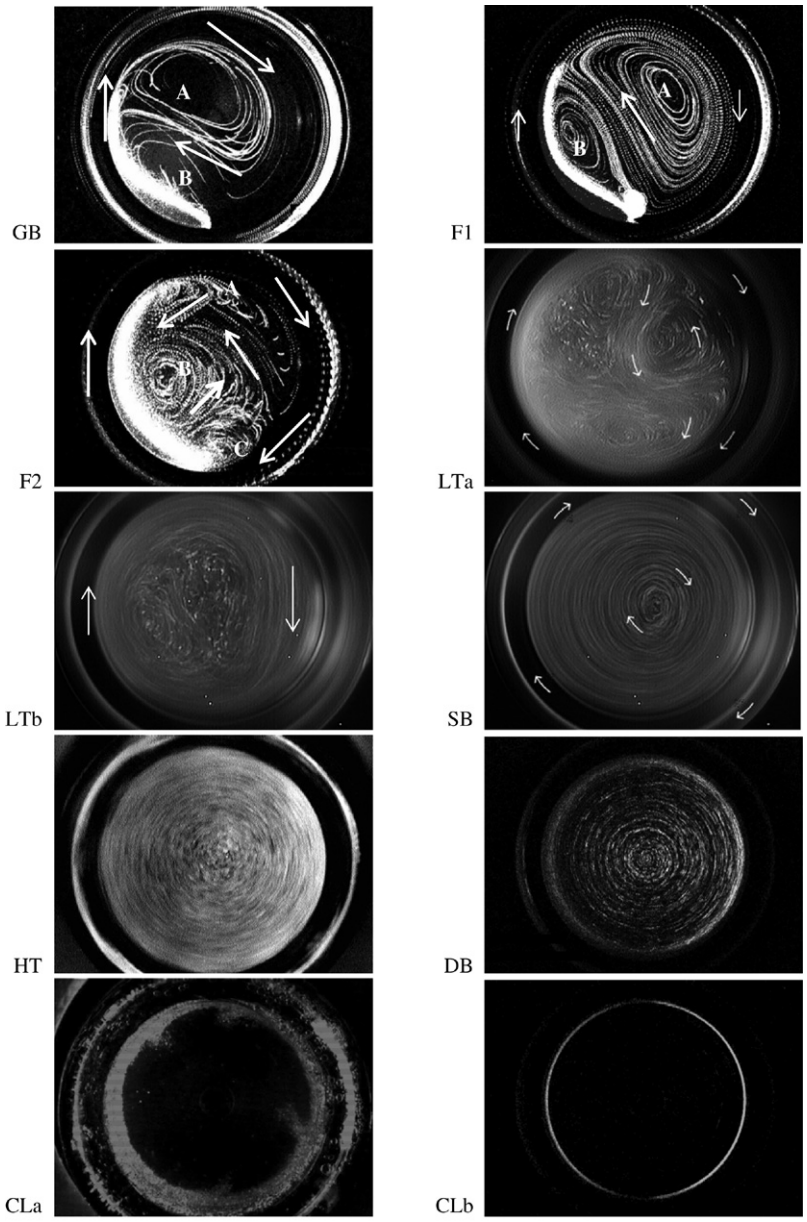

Fig. 4. Cross-sectional view of particle trajectories in the short rotating cylinder. For clarity, 30 sequential images taken at time intervals ranged from 1 s (for low-ω sates) to 1/30 s (for high-ω sates) are superimposed (except (CLa) which is an individual image) and the contrast of the pictures is reversed with white streaks on a black background. The arrows indicate the direction of the local flow and the cylinder rotation. GB: Granular Bed, F1: Fingering flow I, F2: Fingering flow II, LTa: Low-rotation-rate Transition with a remaining granular bed, LTb: Low-rotation-rate Transition without a granular bed, SB: Stable Bands, HT: High-rotation-rate Transition, DB: Discontinuous Banding, CLa: Centrifugal Limit near the transition boundary, and CLb: Centrifugal Limit with all particles on the cylinder wall.

particles remain suspended. The LT phase has a transition character, which is unique when compared with the other phases discussed above. Near the lower-ω boundary, the system behaves more like F2. As the system moves toward the larger-ω boundary, the fingering flow behavior diminishes and the system starts to resemble the Stable Band phase, to be discussed below. The band-like appearance is clearly seen in Fig. 3 (LTb). Particles form periodic bands along the z-axis with a distinct self reinforcing flow structure. Before reaching the transition boundary between the LT and SB phases, however, these bands are unstable and fluctuate both in time and spatial orientation in a quasi-periodic fashion.

Stable Bands (SB)

Once the lower-ω boundary of the SB phase is reached, the fluctuating velocity components parallel to the rotation axis are switched off, and the bands themselves become stationary in space. As shown in Fig. 3 (SB), the bands are structurally identical and are separated alternately by void regions. The position of the bands remains fixed for a given ω with fairly uniform spacing, except near the cylinder ends. The average spacing between the bands is $\lambda = 2.2$ cm, which is 1.2 ± 0.1 times the tube diameter. Lipson et al. [25–27] also reported band formation for nearly neutral buoyant particles in water and other low-viscosity fluids. While their experimental

uncertainties are relatively large, the measured band spacing is comparable to our result.

In a different experiment [23,28], we vary the cylinder diameter by a factor of two. The particle size is also varied by a factor of two and the particle volume fraction ϕ is changed from 1.1% to 2.6%. These measurements reveal that the average band spacing changes only with the cylinder diameter and is independent of other control parameters, such as the solvent viscosity, the rotation rate, and the particle size and concentration. Seiden et al. [26,27] reported that the average band spacing also varies with the cylinder length L. Nevertheless, our measurements carried out in the $L = 22.75$ cm and $L = 2.25$ cm cylinders show that the steady state behavior of the phase diagram for this and other suspensions remains unchanged with L.

Local-structure Drop-off (LD)

At even larger ω, the secondary flow pattern associated with the band structure cannot keep up with the increased cylinder rotation and the band structure decays. At first, one segment of the bands disappears and that region appears uniform at lower particle concentration. The other band segments remain unchanged with little or no adjustment in axial location. However, they may absorb particles to increase the gravitational force required to maintain the remaining structures. This is shown in Fig. 3 (LD). Once the drop-off process starts at a given location, it spreads along the z-axis in both directions with increasing ω. It is found that the local-structure drop-off is a reversible process. Reducing the rotation rate reverses the process and restores any destroyed structures to the original position.

Homogeneous Region (HR)

For high-viscosity solutions, the drop-off process continues with increasing ω until all the bands disappear from the entire cylinder. As shown in Fig. 3 (HR), the spatial distribution of the particles in the HR phase is fairly uniform throughout the cylinder. The HR phase is extremely sensitive to the levelling of the rotating cylinder and a slight tilt of less than a tenth of a degree will result in a notable concentration gradient along the tube length. In the experiment, we were able to keep the cylinder at a perfectly levelled state for several weeks to test the steady state nature of the HR phase. It is seen from Fig. 2 that the HR phase occupies a small island region in phase space, indicating that a delicate balance among the governing forces is required for this particular flow state.

High-rotation-rate Transition (HT)

The High-rotation-rate Transition is characterized by large-scale concentration variations along the rotation axis (z-axis). As shown in Fig. 3 (HT), the particles migrate and form three concentrated (dark) regions extending along the z-axis in this case. The dark regions are several centimeters in length and are separated by two less populated (light) regions. Usually we see two or three concentrated regions along the entire length of the cylinder. There is no obvious secondary flow associated with this structure, as in the case of the SB and LD phases. The exact number and the location of the concentrated regions vary with ω and η but seem to be independent of L. Similar to the situation in the LT phase, the HT phase also resembles a coexistence phase. Near the lower-ω boundary, the system resembles the LD phase with a background concentration variation. As the system moves toward the larger-ω boundary, the concentrated regions shrink and the system behaves more like the DB phase, to be discussed below.

Discontinuous Banding (DB)

As ω increases further, the wide concentrated region in the HT phase contracts to form a very dense region of particles having a width up to one cylinder diameter. Fig. 3 (DB) shows the concentration profile of the DB phase along the z-axis. Hereafter, we refer to these dense regions of particles as segregation bands. The location of the band regions appears random and they evidence no inter-band interaction. High-viscosity suspensions tend to have more but smaller and less developed segregation bands. By comparison, low-viscosity suspensions have fewer but larger and better formed segregation bands. It is seen from Fig. 3 (DB) that the void region between the bands is completely empty of particles. Unlike the bands in the SB phase, the segregation bands have sharp interfaces with the neighboring unpopulated regions, a discontinuous concentration profile at the interface.

Centrifugal Limit (CL)

The large-ω limit of the phase diagram is the centrifugal limit, at which all the particles spin out to the cylinder wall under the influence of the centrifugal force. Given enough time, all patterns present on the cylinder wall are eliminated and a uniform coating layer of particles is generated on the wall. Fig. 3 (CLb) shows the side view of the coating layer of particles on the cylinder wall. The transition from the DB phase to the CL phase is one of the sharpest transitions discussed so far. This transition takes place sharper than our resolution in the rotation period, which is 25 ms per rotation, and is completely reversible. In other words, a change of $<2.5\%$ in rotation period (25 ms out of 1 s at $\eta \simeq 60$ cP) will cause all the particles to spin out to the cylinder wall. Going back to the previous setting will recreate the segregation bands in exactly the same axial locations.

3.2. Secondary flow associated with stable bands

Among the ten different steady states discussed above, the stable band (SB) phase is of particular interest. As mentioned above, secondary flow components parallel to the axis of rotation appear with fingering in the lower-ω boundary of the LT phase. This axial flow continues throughout the phase even as the particle density evidences bands near the larger-ω boundary. What distinguishes this boundary to the SB phase is a switching off of the fluctuating velocity components parallel to the rotation axis, while the large-scale band density distribution persists. Once the lower-ω boundary of the SB phase is reached, the self reinforcing secondary flow pattern associated with the band structure stabilizes and the bands themselves become stationary in space.

To characterize the particle concentration variation along the z-axis more quantitatively, we convert the two-dimensional

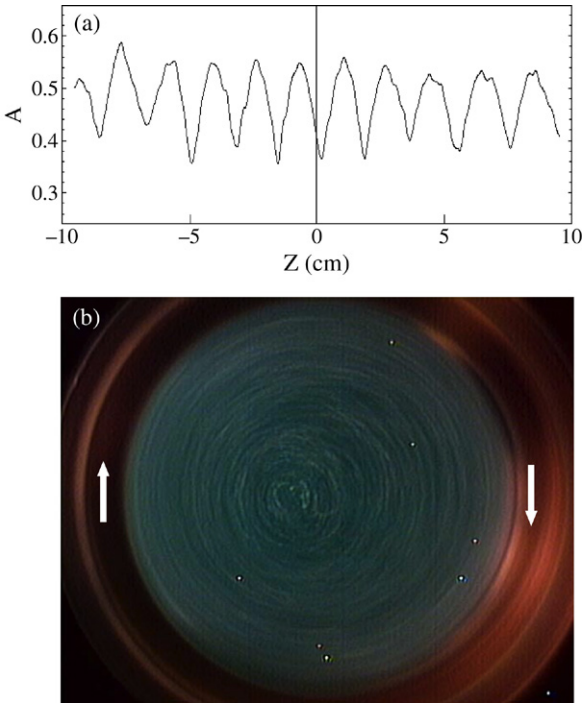

Fig. 5. (a) Measured absorption coefficient A of the transmitted light as a function of the axial position z in the stable band phase. The transmitted light intensity has been averaged over the cylinder diameter and the vertical line at $z = 0$ indicates the middle of the cylinder. (b) (color online) Cross-sectional view of particle trajectories in the stable band phase. The pictures are taken in the dense band region with the highest particle concentration. For clarity, 30 sequential images taken at time interval of 1/10 s are superimposed. The arrows indicate the direction of the cylinder rotation. There are a few small defect spots on the optical window, which appear as stationary bright spots in the picture when the intensity of the illuminating light sheet is low. A solid state laser of wavelength 532 nm is used to generate the illuminating light sheet.

image files into one-dimensional intensity profiles by averaging out a vertical column of pixels in each of the individual images shown in Fig. 3 to obtain the column-averaged transmitted light intensity $\bar{I}(z)$ as a function of the axial position z. Because the scattering and absorption of the incident light are proportional to the number of particles in the optical path (for vanishing ϕ), the measured intensity profile $\bar{I}(z)$ provides information about the particle concentration profile along the z-axis. Fig. 5(a) shows the normalized intensity profile of the transmitted light along the z-axis. In the plot, the absorption coefficient A is define as

$$A = \frac{I_s - \bar{I}(z)}{I_s}, \tag{2}$$

where $I_s = 255$ is the saturation intensity of the CCD camera used in the experiment. With this definition, darker regions with more particles will have a larger value of A.

It is seen from Fig. 5(a) that the particle concentration profile has a sharp triangular waveform (which is also directly visible from a top view of the sample cell). The particle distribution inside each band is symmetric about its central peak position. These maximum concentration planes are stationary in space and the velocities at these locations are vertical and parallel with each other. As shown in Fig. 5(b) [and in Fig. 4 (SB)], the particle trajectories in the r–θ plane become exclusively clockwise in the SB phase. The "center" of the particle trajectories, however, does not coincide with the axis of rotation. The trajectory center follows a zigzag path as a function of z, being closer to the upgoing wall in the r–θ planes with the highest particle concentration [as shown in Fig. 5(b)] and closest to the downgoing wall at the smallest particle concentrations.

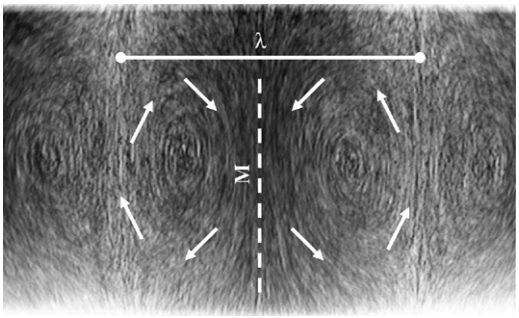

Fig. 6. Side view of the velocity field inside a stable band. For clarity, 30 sequential images taken at 1/30 s intervals are superimposed and darker regions have more particles. The vertical dashed line M indicates the r–θ plane with the highest particle concentration and the arrows indicate the direction of the local flow. The horizontal solid line λ indicates the beginning and ending edges of a single band cell.

Fig. 6 shows a side view of the velocity field inside a stable band. The vertical dashed line M indicates the r–θ plane with the highest particle concentration. It is seen that the velocity field is symmetric about the maximum concentration line. On each side of line M, each particle orbits on its own axis, which tilts at an angle with respect to the rotation axis and points out of the plane of the image toward the less populated band region. The arrows in Fig. 6 indicate the direction of the local flow. Particles are drawn into the dense band region by the secondary flow. Evidently this increased particle concentration produces a larger downward velocity and reinforces the secondary flow.

4. Discussion

The above experimental results clearly demonstrate that the rotating suspension is a complex system and has many experimental parameters. They include the rotation rate ω, solvent viscosity η, particle radius a, volume fraction ϕ, cylinder length L and radius R. These parameters give rise to multiple velocity and time scales for the system. Without a theory, it is difficult to know what are the dimensionless control parameters for the system. As a result, one has a huge parameter space to explore experimentally. In fact, several independent experiments have been carried out recently in different rotating suspensions.

The experiments by Seiden et al. [25–27] focused on the study of band formation. They measured the average band spacing λ as a function of the ratio of the cylinder length L to the cylinder radius R. The suspension system used in the experiments consisted of millimeter-sized particles dispersed in water or other low-viscosity fluids. A complication caused by using the large particles is that the Reynolds number based on

the particle size and the settling velocity, $Re_1 = 2aU_0\rho_s/\eta$, becomes very large. For example, the values of Re_1 for the polystyrene and silica spheres used in the experiment are in the range between 6.5 and 735. In this case, the inertial effect of the individual particles becomes significant.

Breu et al. [29,30] studied concentration patterns formed in the rotating suspension of glass beads. In one experiment [29], they investigated how the uniform monolayer of particles coated on the inner wall of the rotating cylinder under the influence of strong centrifugal force at high rotation rate develops an instability, when the rotation rate is reduced below a critical value. Such an instability causes the particle layer to collapse and form radially symmetric rings on the inner wall. This transition is similar to that between the DB and CL phases, as discussed in Section 3.1. We notice that the experiment by Breu et al. was carried out in a different region of parameter space, because the particle based Reynolds number for the suspension of 300 μm diameter glass beads in water is large ($Re_1 \simeq 20$).

In another experiment [30], Breu et al. found "travelling waves" in a rotating suspension of 300 μm diameter glass beads in an aqueous solution of glycerin. Given our results, though in a different region of parameter space, we postulate that the onset of the travelling waves reported by Breu et al. is associated with the transition from the F1 to F2 phases. Because narrow strip images (512 × 2 pixels) were used for flow visualization, only the axial (horizontal) motion of a thin horizontal layer of particles was recorded and the three-dimensional structure of the concentration and velocity fields was not studied in the experiment by Breu et al.

There is an important question about what the appropriate dimensionless control parameters are for the rotating suspensions. While the experiments discussed above [25–27,29,30] revealed several interesting concentration and flow patterns in the system, they were conducted only in an isolated and rather limited parameter space. Theoretical arguments and calculations [25–27,29–32] have been made to explain the observed flow patters, but they have different assumptions and predictions. A generally accepted theoretical framework for the rotating suspension is yet to obtain. Therefore, it becomes essential to conduct careful and systematic measurements over a wide range of parameter space. These measurements can provide us an overall picture for the rich dynamics of the system, so that further theoretical analysis can be carried out to give specific guidelines and predictions for the experiment. In the experiment discussed in Section 3, we carefully studied the overall phase diagram of the system and mapped out the transition boundaries between different phases over a wide range of the rotation rate ω and solvent viscosity η for fixed values of particle radius a, volume fraction ϕ, and cylinder radius R [17,18]. New experiments are carried out looking at the influence of a, ϕ and R on the phase behavior of the rotating suspension. The results will be reported elsewhere [23,28].

4.1. Dimensional analysis

While we have not been able to verify experimentally a unique set of dimensionless parameters for the system, the experimental results obtained so far have provided adequate information for us to carry out a simple dimensional analysis based on the two-fluid model [33,34]. The macroscopic equations of motion for the rotating suspension are taken to be the conservation equation of mass and the Navier–Stokes equation. In the rotating frame with angular velocity $\vec{\omega}$, at which the entire rotating system is at rest, the equations of motion for the suspension with variable density $\rho(\mathbf{r}, t)$, pressure $P(\mathbf{r}, t)$, and velocity $\mathbf{U}(\mathbf{r}, t)$ take the following form [26,35]

$$\partial_t \rho + \nabla \cdot (\rho \mathbf{U}) = 0, \tag{3}$$

$$\rho \partial_t \mathbf{U} + \rho \mathbf{U} \cdot \nabla \mathbf{U} = -\nabla P + \eta \nabla^2 \mathbf{U} + \rho \mathbf{g} - \vec{\omega} \times (\vec{\omega} \times \rho \mathbf{r}) - 2(\vec{\omega} \times \rho \mathbf{U}), \tag{4}$$

where $\mathbf{g}$ is the gravitational acceleration. The last two terms on the right hand side of Eq. (4) are, respectively, the centrifugal and Coriolis forces.

Two additional equations similar to Eqs. (3) and (4) can be written for the particles with volume fraction $\phi(\mathbf{r}, t)$, pressure $\Pi(\mathbf{r}, t)$, and velocity $\mathbf{V}(\mathbf{r}, t)$. The density of the suspension is related to the volume fraction of the particles via $\rho = \rho_s + \Delta\rho\phi$, where $\Delta\rho = \rho_p - \rho_s$ is the density difference between the particle (ρ_p) and the solvent (ρ_s). The pressure term in Eq. (4) can be eliminated by taking the curl on both sides of the equation. At this point we have four equations and four unknowns, and the remaining problem is to solve the four coupled (non-linear) equations, which is still a formidable task.

To further simplify the equations, one needs to compare the relative weight of each of the force terms as well as the non-linear terms in Eq. (4). It is seen from Fig. 2 that the rotating suspension has rich dynamics and exhibits a total of ten different phases. This suggests that the balance among various driving forces is different for different phases. For example, at low rotation rates the dynamics of the F1 and F2 phases are determined primarily by the settling of the particle chains or fingers (gravity dominant). At very high rotation rates, however, the centrifugal force becomes dominant and all the particles are spun onto the cylinder wall. Therefore, the dimensional analysis has to be specific and a universal analysis applied to all the phases seems unlikely.

In the following we limit our analysis on the stable band (SB) phase. From Fig. 2 we choose a typical point in the SB phase with $\omega \simeq 2\ \mathrm{s}^{-1}$ and $\nu \simeq \eta/\rho_s \simeq 0.35\ \mathrm{cm}^2/\mathrm{s}$. The centrifugal force $\vec{\omega} \times (\vec{\omega} \times \rho\mathbf{r})$ scales as $\rho\omega^2 R$. The velocity $\mathbf{U}$ in Eq. (4) is the relative velocity with respect to the uniform rotation. By watching the motion of the bands over a period of time, we find that the rotation rate of the fluid in the SB phase is approximately the same as that of the cylinder. However, because of variations of the particle concentration, the rotation center of the particle trajectories is shifted by an amount of ΔR relative to the rotation axis of the cylinder. This is clearly shown in Fig. 5(b). As a result, the relative velocity scales as $|\mathbf{U}| \equiv U \simeq \omega\Delta R$. For a single (heavy) particle in a uniform rotating fluid, this relation holds exactly [16,27]. The typical length scale associated with U is the cylinder radius R. The ratio of this relative velocity to the mean rotation velocity is thus $U/(\omega R) \simeq \Delta R/R$. From Fig. 5(b) we find that the typical value of $\Delta R/R$ in the SB phase is $\Delta R/R \simeq 0.16$.

With these experimental values, we now can estimate the relative weight of various terms in Eq. (4). The Reynolds number Re_r, which is a ratio of the non-linear term to the viscous force, is given by $Re_r = \rho\mathbf{U}\cdot\nabla\mathbf{U}/(\eta\nabla^2\mathbf{U}) \simeq UR/\nu \simeq 0.8$. The Rossby number Ro, which is a ratio of the non-linear terms to Coriolis force, is given by $Ro = \rho\mathbf{U}\cdot\nabla\mathbf{U}/(2\vec{\omega}\times\rho\mathbf{U}) \simeq U/(2\omega R) \simeq 0.08$. Therefore, the non-linear terms in Eq. (4) can be ignored. The ratio of Coriolis force to the gravitational force is given by $2(\vec{\omega}\times\rho\mathbf{U})/(\rho g) \simeq (2\Delta R/R)(\omega^2 R/g) \simeq 1.2\times10^{-3}$, suggesting that Coriolis force is less important when compared with the gravitational force. Finally, we compare the centrifugal force with the gravitational force. The ratio of the centrifugal force to the gravitational force is given by $(\vec{\omega}\times(\vec{\omega}\times\rho\mathbf{r})/(\rho g) \simeq \omega^2 R/g \simeq 3.9\times10^{-3}$, suggesting that in the SB phase the centrifugal force is less important than the gravitational force.

From the above numerical estimations, we simplify Eqs. (3) and (4) into the following form

$$\partial_t\rho + \nabla\cdot(\rho\mathbf{U}) = 0, \tag{5}$$

$$\rho\partial_t\mathbf{U} = -\nabla P + \eta\nabla^2\mathbf{U} + \rho\mathbf{g}, \tag{6}$$

where $\rho\mathbf{g}$ becomes the only remaining external force. Because both the centrifugal and Coriolis forces are ignored, Eqs. (5) and (6) are also valid in the laboratory frame, in which the cylinder wall is rotating (as a boundary condition) but the gravitational acceleration $\mathbf{g}$ becomes time independent. By non-dimensionalizing Eqs. (5) and (6) with respect to the length R, the velocity $R\omega$, and the solvent density ρ_s, we have

$$\rho\partial_t\mathbf{U} - A[\rho\hat{\mathbf{y}} - \nabla P] + \frac{1}{Re_3}\nabla^2\mathbf{U} \simeq 0, \tag{7}$$

$$\partial_t\rho + \nabla\cdot\rho\mathbf{U} \simeq 0, \tag{8}$$

where $A = g/(R\omega^2)$ is a ratio of the gravitational acceleration to the centripetal acceleration, $\hat{\mathbf{y}}$ is a unit vector pointing to the direction of $\mathbf{g}$, and $Re_3 = \omega R^2\rho_s/\eta$ is the Reynolds number. The time derivative terms are kept because the motion of the suspension in the rotating frame is under the influence of an alternating gravitational force $\rho\mathbf{g}$ of frequency γ. In Eqs. (7) and (8), all the flow variables (ρ, $\mathbf{U}$, P) and the coordinates ($\mathbf{r}$, t) are dimensionless. With the above scaling variables, the pressure P is scaled by $\rho_s g R$.

The above analysis suggests that the dynamics of the rotating suspension is determined by two dimensionless parameters. The first parameter is A, which can be rewritten as

$$F_1 = \frac{\Delta\rho g}{\rho_s\omega^2 R}, \tag{9}$$

where F_1 is a ratio of the effective acceleration of gravity for the particles in the suspension to the centripetal acceleration of the solution at the cylinder wall. The second parameter is the Reynolds number Re_3 based on the cylinder radius R and the wall speed $R\omega$. Fig. 7 is a replot of the phase diagram shown in Fig. 2 as a function of $\log_{10}F_1$ and $\log_{10}Re_3$. It is seen that the curved phase boundaries in the linear plot shown in Fig. 2 become almost linear, as indicated by the dashed lines in the log–log plot in Fig. 7. The linear behavior in the log–log plot suggests that the phase boundaries can be described by an effective power law, $F_1 \sim (Re_3)^{\epsilon}$.

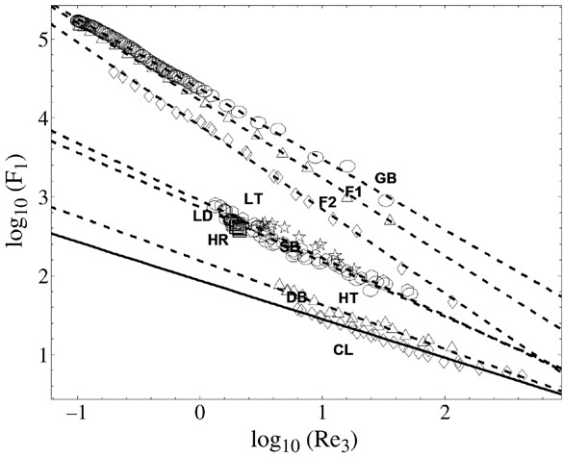

Fig. 7. Replot of the phase diagram shown in Fig. 2 as a function of $\log_{10}F_1$ and $\log_{10}Re_3$. The symbols show the experimentally determined phase boundaries and the dashed lines indicate the linear behavior of each phase boundary in the log–log plot. The solid line is the power-law fit, $F_1 = 87.85(Re_3)^{-0.49}$, to the diamonds.

For example, the solid line in Fig. 7 shows a power-law fit to the phase boundary between DB and CL. From the fit, we find $\epsilon = 0.49$. It is also seen from Fig. 7 that the measured phase boundaries form three distinct groups. The three low-rotation-rate boundaries form a group; the two large-rotation-rate boundaries form another group; and the remaining intermediate rotation rate boundaries form a third group. It should be pointed out that the actual variables used in Fig. 7 are $1/\omega^2$ and ω/η (or η/ω). All the other parameters in Eqs. (9) and (7) remain constant in the experiment. To verify a unique set of dimensionless parameters experimentally, one needs to change the value of other experimental parameters for the system, such as the particle radius a, cylinder radius R, volume fraction ϕ, and density difference $\Delta\rho$. A systematic variation of the experimental parameters will allow us to have a better understanding of the overall dynamics of the system. It will also facilitate further quantitative characterization of the flow structures discussed in Section 3.

4.2. A simple solution for stable bands

As mentioned above, Eqs. (7) and (8) contain three unknowns [$\rho(\mathbf{r},t)$, $P(\mathbf{r},t)$ and $\mathbf{U}(\mathbf{r},t)$] and need to be solved together with two additional equations for the particles [33, 34]. Eqs. (7) and (8) become decoupled from the equations of motion for the particles when the density profile of the suspension, $\rho = \rho_s + \Delta\rho\phi$, is known. Based on the observations shown in Figs. 3 (SB) and 5(a), we postulate a general density solution for the SB phase and solve for the velocity field $\mathbf{U}(\mathbf{r},t)$. The solutions (ρ, U) may be used (as source terms) in the remaining two equations, with which one solves for $\mathbf{V}(\mathbf{r},t)$ and $\Pi(\mathbf{r},t)$. We have not found nor are we guaranteed that these solutions can be found. Nevertheless, the solutions that we find below describe the fluid motion in the SB phase well.

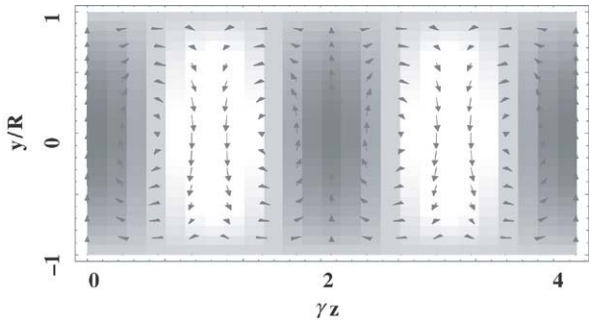

Fig. 8. Calculated velocity vector map in a vertical plane passing through the axis of rotation of the cylinder. The arrows indicate the direction and magnitude of the velocity vector field. The concentration distribution of the particles is indicated by the grey level, which is reversed for clarity with lighter regions having more particles.

With the non-slip boundary conditions, Eqs. (7) and (8) admit the following steady state band solution in the cylindrical coordinates:

$$\rho(r,\theta,z) = 1 + f(r)\cos(\gamma z)$$
$$\mathbf{U}(r,\theta,z) = [U_r(r)\sin(\theta)\cos(\gamma z), r + U_\theta(r)\cos(\theta)\cos(\gamma z), U_z(r)\sin(\theta)\sin(\gamma z)], \quad (10)$$

where

$$f(r) = Re_3 A\gamma \frac{2\gamma I_0(\gamma) + [\gamma^2(r^2-1) - 6]I_1(\gamma)}{2 - 2I_0(\gamma) + \gamma I_1(\gamma)}$$
$$U_r(r) = U_\theta(r) = \frac{-2I_0(\gamma) + 2I_0(\gamma r) - (r^2-1)\gamma I_1(\gamma)}{2 - 2I_0(\gamma) + \gamma I_1(\gamma)}$$
$$U_z(r) = -\frac{1}{\gamma}\frac{\mathrm{d}U_r(r)}{\mathrm{d}r}. \quad (11)$$

In the above, $I_n(\gamma)$ is the modified Bessel function of the first kind and γ is a dimensionless wave number for the band structure, which will be determined below.

While other density profiles may give different velocity distributions, the solution shown in Eqs. (10) and (11) proves instructive for our purposes. It is clearly seen from Figs. 3 (SB) and 5(a) that the proposed density profile $\rho(r,\theta,z)$ in Eq. (10) is the dominant mode of the actual distribution. This density profile produces a two-dimensional flow in the vertical plane passing through the axis of rotation of the cylinder (side view), in addition to the imposed flow in the r–θ plane (end view). Fig. 8 shows the side view of the calculated velocity vector map of two band cells. In the densely populated regions (lighter regions) the secondary flow is downward and upward in the least densely populated regions (darker regions). As shown in Fig. 6, the velocity field within a band cell is symmetric about the central line (r–θ plane) of maximum concentration. Particles are drawn into the dense band region by the secondary flow. This increased particle concentration produces a larger downward velocity and reinforces the secondary flow. These characteristic features are also observed in Fig. 8.

Fig. 9 shows the cross-sectional view of the calculated velocity field in two different r–θ planes. The superposition of the secondary and applied flows evidences a circulation

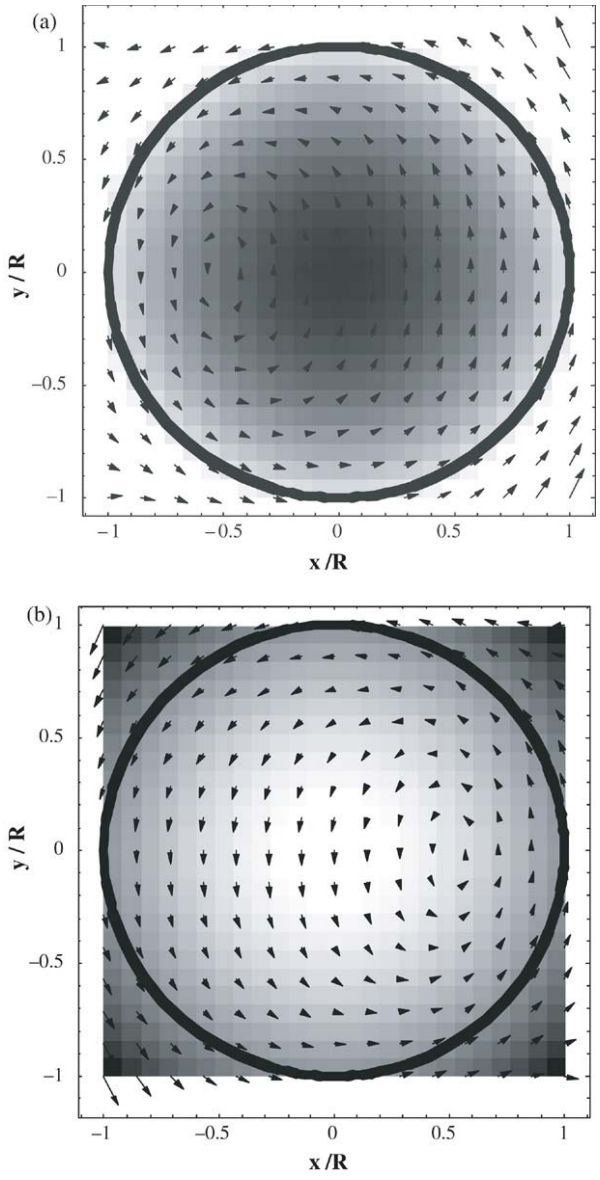

Fig. 9. Calculated velocity vector map (a) in the r–θ plane with minimum particle concentration and (b) in the r–θ plane with maximum particle concentration. The arrows indicate the direction and magnitude of the velocity vector field. The concentration distribution of the particles is indicated by the grey level, which is reversed for clarity with lighter regions having more particles.

in the direction of the imposed flow but with the center of rotation offset horizontally from the rotation axis. In the r–θ planes with the highest particle concentration [see Fig. 9(b)] the center is shifted toward the upgoing wall, and in the least dense r–θ planes [see Fig. 9(a)] it is shifted toward the downgoing wall. The range of the horizontal shift is determined by the ratio of the secondary circulation velocity to the rotation rate of the cylinder. As discussed in Section 3.2, a similar zigzag migration of the rotation axis of the particle trajectories along the cylinder is observed in the experiment and is explained as the superposition of the two flows [17,18].

With the analytic band solution shown in Eqs. (10) and (11), one can calculate the viscous dissipation rate σ as a function

$$\sigma = \int_0^1 r\mathrm{d}r \int_0^{2\pi} \mathrm{d}\theta \int_0^{2\pi/\gamma} \mathrm{d}z (2\eta \nabla \mathbf{U}^s : \nabla \mathbf{U}^s)$$
$$= \frac{1}{2}\eta\pi^2 \left[\frac{81\gamma I_0^2(\gamma) + (-132/\gamma + 21\gamma + 2\gamma^3) I_1^2(\gamma) + 3\gamma I_2^2(\gamma) - 12 I_0(\gamma)[(8+\gamma^2) I_1(\gamma) + \gamma I_2(\gamma)]}{6[2 - 2I_0(\gamma) + \gamma I_1(\gamma)]^2} \right.$$
$$\left. + \frac{-3I_1(\gamma)[64 I_2(\gamma) + 25\gamma I_3(\gamma)] + 12[3\gamma I_1^2(\gamma) - 2I_2(\gamma)(\gamma I_0(\gamma) + 4I_1(\gamma))]}{6[2 - 2I_0(\gamma) + \gamma I_1(\gamma)]^2} \right], \quad (12)$$

of the band wave number γ [36]: using Eq. (12) where

$$\nabla \mathbf{U}_{ij}^s = \frac{1}{2}\left(\frac{\partial U_i}{\partial x_j} + \frac{\partial U_j}{\partial x_i}\right) - \frac{1}{3}\delta_{ij} \sum_{k=1}^{3} \frac{\partial U_k}{\partial x_k} \quad (13)$$

is the symmetric part of the velocity gradient tensor $\nabla \mathbf{U}$ with zero trace, and $\nabla \mathbf{U}^s : \nabla \mathbf{U}^s$ denotes the contraction of the two tensors into a scalar.

In fact, the dissipation in a rotating suspension contains two contributions. The first one is due to fluid shear, which is calculated in Eq. (12). The second contribution comes from particles slipping through the solvent. Because both the volume fraction of the particles and the relative velocity between the particles and the solvent are small, the latter part of the dissipation is negligible. This dissipation is essentially the same for all band structures, since each particle settles with respect to the local solvent regardless of the global structure of the suspension. Because it results from the solution of the (coupled) linear equations shown in Eqs. (7) and (8), the calculated σ in Eq. (12) (or the entropy production rate σ/T, where T is temperature) is expected to be minimized [37]. Thus the dissipation rate may be used to select the wavelength for the banding velocity distribution. In Eq. (12), the dissipation rate σ is computed over one complete band period. To compare band structures with different wave numbers, we divide σ by the band wavelength and obtain a normalized dissipation rate per unit length $\gamma_0 = \gamma\sigma/(2\pi)$. Fig. 10(a) shows the calculated $4\pi\gamma_0/\eta$ as a function of the normalized band wavelength λ/R $(=2\pi/\gamma)$. The minimum dissipation occurs for a band wavelength $\lambda_m \simeq 2.44R$. This value is in excellent agreement with the measured value of $\lambda_m \simeq 2.4R$ [17,18].

Seiden et al. [26,27] have shown that for a given cylinder of length L, the wavelength λ of the bands formed along the cylinder satisfies the condition $L = n\lambda/2$, where $n = 2, 3, \ldots$, is an integer. For a given stable band configuration, if the cylinder length L is increased, the system has freedom to increase either the band wavelength λ or the number of bands $n/2$, in order to satisfy the above condition. In Fig. 10(b), we show the calculated $4\pi\gamma_0/\eta$ as a function of L/R $[= 2\pi n/(2\gamma)]$ for $n/2 = 9$, 9.5, 10 and 10.5, respectively (from left to right). As the cylinder length L increases, a different number of bands or half bands is predicted to occur at $L/R \simeq$ 22.6, 23.8 and 25.0, based on the minimum dissipation rate. This transitional behavior of the band numbers is in good agreement with the experimental observations made by Seiden et al. [26,27]. Given accurate velocity presentations for the ten steady states discussed in Section 3.1, we could test minimum dissipation as a predictor of the transition from one state to another.

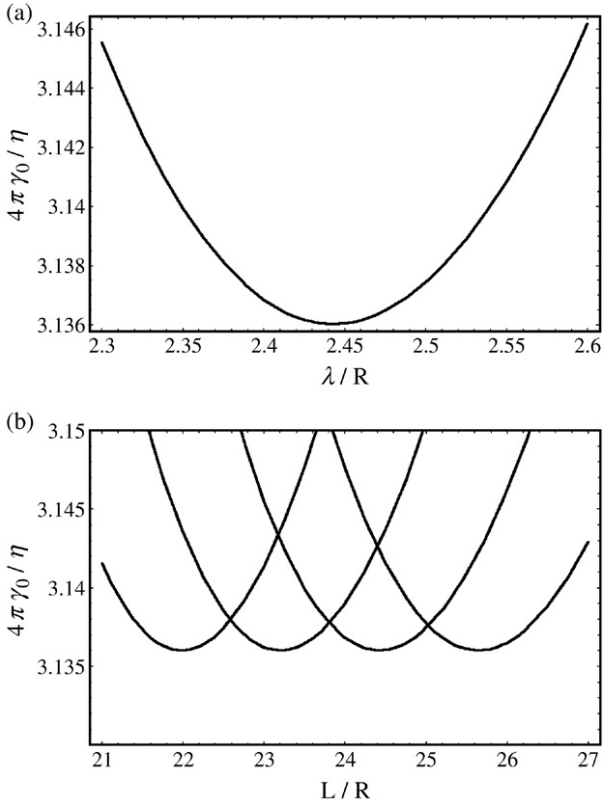

Fig. 10. (a) Calculated $4\pi\gamma_0/\eta$ as a function of the normalized band wavelength λ/R. (b) Calculated $4\pi\gamma_0/\eta$ as a function of the normalized cylinder length $L/R = 2\pi n/(2\gamma)$ for $n/2 = 9$, 9.5, 10 and 10.5, respectively (from left to right).

5. Summary

We have carried out a systematic study of concentration and velocity patterns formed in a suspension of non-Brownian settling particles completely filled in a horizontal rotating cylinder. Individual flow states, or phases, are studied using both side and cross-sectional imaging to examine the detailed flow structures. The system exhibits a total of ten different steady states and their transition boundaries are mapped out over a wide range of the rotation rate ω and solvent viscosity η.

Although the accurate determination of the phase boundaries is a tedious and lengthy process, such an effort is essential for the understanding of the overall dynamics of the system and the mechanism of transition between different phases. The experiment suggests that the large number of patterns and rich dynamics found in the rotating suspension come from the interplay among the viscous drag, gravitational force, and centrifugal force.

A dimensional analysis on the equations of motion is carried out for the rotating suspension. It is found that the dynamics of the stable band phase is determined primarily by two dimensionless parameters: the Reynolds number Re_3 based on the cylinder radius R and the wall speed $R\omega$ and the ratio A of the gravitational acceleration g to the centripetal acceleration $R\omega^2$. Curved phase boundaries in the linear plot become straight lines when the transition boundaries are plotted on log–log scales over the two scaling variables. On the basis of the experimental observations, we postulate a general concentration profile for the particles in the stable band phase and find a solution for the velocity field $\mathbf{U}(\mathbf{r}, t)$. The characteristic features of the calculated $\mathbf{U}(\mathbf{r}, t)$ agree well with the experiment. Furthermore, using the analytic band solution $\mathbf{U}(\mathbf{r}, t)$, we calculate the viscous dissipation rate as a function of the band wavelength. Minimizing the calculated dissipation rate gives rise to a unique value of the band wavelength, which is in excellent agreement with the experiment. A further theoretical analysis is needed to explain the dynamic behavior of other steady states of the system.

Acknowledgements

We thank Anthony J.C. Ladd for useful discussions and communications. This work was supported in part by the Research Grants Council of Hong Kong SAR under Grant No. HKUST603504 (P.T).

References

[1] M.E. Cates, M.R. Evans, Soft and Fragile Matter, IoP Publishing, Bristol, UK, 2000.
[2] W.B. Russel, D.A. Saville, W.R. Schowalter, Colloidal Dispersions, Cambridge University Press, Cambridge, UK, 1989.
[3] J.P. Hansen, I.R. McDonald, Theory of Simple Liquids, 2nd edition, Academic Press, Orlando, USA, 1986.
[4] A.P. Gast, W.B. Russel, Phys. Today 51 (1998) 24.
[5] W.B. Russel, Nature 421 (2003) 490.
[6] P.N. Pusey, W. van Megen, Nature 320 (1986) 340.
[7] D.G. Grier, C.A. Murray, J. Chem. Phys. 100 (1994) 9088.
[8] A. van Blaaderen, P. Wiltzius, Science 270 (1995) 1177.
[9] W.K. Kegel, A. van Blaaderen, Science 287 (2000) 290.
[10] E.R. Weeks, J.C. Crocker, A.C. Levitt, A. Schofield, D.A. Weitz, Science 287 (2000) 627.
[11] U. Gasser, E.R. Weeks, A. Schofield, P.N. Pusey, D.A Weitz, Science 292 (2001) 258.
[12] A. Yethiraj, A. van Blaaderen, Nature 421 (2003) 513.
[13] H. Lekkerkerker, Soft and Fragile Matter, IoP Publishing, Bristol, UK, 2000, p. 305.
[14] J. Happel, H. Brenner, Low Reynolds Number Hydrodynamics, Kluwer Academic Publishers, Dordrecht, The Netherlands, 1963.
[15] J. Crocker, D.G. Grier, J. Colloid Interface Sci. 179 (1996) 298.
[16] G.O. Roberts, D.M. Kornfeld, W.W. Fowlis, J. Fluid Mech. 229 (1991) 555.
[17] W.R. Matson, B.J. Ackerson, P. Tong, Phys. Rev. E 67 (2003) 050301(R).
[18] W.R. Matson, B.J. Ackerson, P. Tong, Phys. Rev. E 71 (2005) 031401.
[19] M.C. Roco, Particulate Two-Phase Flow, Butterworth-Heinemann, Boston, MA, 1996.
[20] U. Schaflinger, Flow of Particles in Suspensions, Springer-Verlag, Wien, New York, 1996.
[21] C. Crowe et al., Multiphase Flows with Droplets and Particles, CRC, Boca Raton, 1998.
[22] S.G. Lipson, J. Phys.: Condens. Matter 13 (2001) 5001.
[23] W.R. Matson, Doctoral Dissertation, Oklahoma State University, 2004 (available at http://physics.ust.hk/penger/Matson.pdf).
[24] S.T. Thoroddsen, L. Mahadevan, Exp. Fluids 23 (1997) 1.
[25] S.G. Lipson, G. Seiden, Physica A 314 (2002) 272.
[26] G. Seiden, S.G. Lipson, J. Franklin, Phys. Rev. E 69 (2004) 015301(R).
[27] G. Seiden, M. Ungarish, S.G. Lipson, Phys. Rev. E 72 (2005) 021407.
[28] W.R. Matson, B.J. Ackerson, P. Tong, J. Fluid Mech (submitted for publication).
[29] A.P.J. Breu, C.A. Kruelle, I. Rehberg, Europhys. Lett. 62 (2003) 491.
[30] A.P.J. Breu, C.A. Kruelle, I. Rehberg, Eur. Phys. J. E 13 (2004) 189.
[31] J. Lee, J.C. Ladd, Phys. Rev. Lett. 89 (2002) 104301.
[32] J. Lee, J.C. Ladd, Phys. Rev. Lett. 95 (2005) 048001.
[33] P.R. Nott, J.F. Brady, J. Fluid Mech. 275 (1994) 157.
[34] M. Ungarish, Hydrodynamics of Suspensions, Springer-Verlag, Berlin, 1993.
[35] D.J. Tritton, Physical Fluid Mechnics, 2nd edition, Clarendon Press, Oxford, UK, 1988, p. 215.
[36] S.R. de Groot, P. Mazur, Non-equilibrium Thermodynamics, Dover, New York, 1984.
[37] G.K. Batchelor, An Introduction to Fluid Mechanics, Cambridge University Press, Cambridge, UK, 1967.